## Multi-Messenger Measurements of the Static Structure of Shock-Compressed Liquid Silicon at 100 GPa

H. Poole, <sup>1,\*</sup> M. K. Ginnane, <sup>2,3</sup> M. Millot, <sup>4</sup> G. W. Collins, <sup>2</sup> S. X. Hu, <sup>2</sup> D. Polsin, <sup>2</sup> R. Saha, <sup>5</sup> J. Topp-Mugglestone, <sup>1</sup> T. G. White, <sup>5</sup> D. A. Chapman, <sup>6</sup> J. R. Rygg, <sup>2,3</sup> S. P. Regan, <sup>2</sup> and G. Gregori <sup>1</sup> Department of Physics, University of Oxford, Oxford OX1 3PU, UK <sup>2</sup> Laboratory for Laser Energetics, University of Rochester, Rochester, New York 14623, USA <sup>3</sup> Department of Mechanical Engineering, University of Rochester, Rochester, New York 14611, USA <sup>4</sup> Lawrence Livermore National Laboratory, Livermore, CA 94550, USA <sup>5</sup> Department of Physics, University of Nevada, Reno, Nevada 89557, USA <sup>6</sup> First Light Fusion Ltd, Unit 9/10 Mead Road, Oxford Pioneer Park, Yarnton, Oxford OX5 1QU, UK (Dated: December 22, 2023)

Ionic structure of high pressure, high temperature fluids is a challenging theoretical problem with applications to planetary interiors and fusion capsules. Here we report a multi-messenger platform using velocimetry and *in situ* angularly and spectrally resolved X-ray scattering to measure the thermodynamic conditions and ion structure factor of materials at extreme pressures. We document the pressure, density, and temperature of shocked silicon near 100 GPa with uncertainties of 6%, 2%, and 20%, respectively. The measurements are sufficient to distinguish between and rule out some ion screening models.

With the advent of high-power lasers, a laboratory-based exploration into extreme states of matter, such as those found in planetary interiors [1] or during asteroid impacts [2], has been realized. This exotic state, referred to as warm dense matter (WDM) [3], is characterized by temperatures and pressures on the order of 1,000 K and 100 GPa. Experimental measurement of material behavior and structure under such conditions is paramount for testing theoretical models used in the pursuit of fusion energy [4, 5] and for modeling planetary phenomena [6–9], where dynamic geophysics processes are dominated by changes in solid- and liquid-state structure.

Over the last few decades, high-energy density (HED) facilities have generated sufficiently long-lived WDM sates, enabling the deployment of advanced diagnostic suites [10–12]. Notably, the Linac Coherent Light Source's X-ray free electron laser (XFEL) has facilitated high-resolution X-ray scattering measurements for probing the electronic and atomic structure of high-pressure states [13, 14]. However, XFELs face limitations in compression capabilities and achievable WDM volumes, hindering the creation of macroscopic homogeneous conditions. At kJ- to MJ-class laser facilities, conditions expected in both Jovian planet interiors [15] and fusion ignition capsules [16] can be generated. Accurately determining pressure, density, and temperature within these complex states of matter remains challenging without employing molecular-dynamic simulations in the data analysis. Furthermore, limitations in applying standard model approximations at high pressures make equation-of-state (EOS) development [17, 18] costly.

Probing shock-compressed matter often relies on single diagnostics e.g. X-ray Thomson scattering (XRTS) [19–22] or X-ray diffraction (XRD) [23–26] for measuring the electronic and atomic structures, or impedance matching techniques via a velocity interferometry system for any

reflector (VISAR) [27]. Initial efforts to combine scattering and velocimetry observations to infer WDM conditions were undertaken by Falk et al. [28], though this required fielding each diagnostic on separate shots. These efforts highlight the critical need for platforms equipped with multiple in situ probing diagnostics.

In this work, an experimental platform was designed to investigate the extreme states of matter generated at high-power laser facilities. We demonstrate a crucial step forward in the endeavor to directly measure pressure, density and temperature of WDM through a multimessenger approach. The simultaneous in situ structure characterization provides a unique tool for controlling diagnostic biases, measurement uncertainties, and selecting models. Reverse Monte Carlo techniques are employed to determine the shock-compressed conditions via measurement of liquid scattering. For this study, silicon was chosen due to its importance in the understanding of planetary interiors [29, 30], for its use as a dopant to ablators in inertial confinement fusion target designs [31, 32] and to mitigate laser-imprint effects on multi-layer targets [33, 34].

The experiments were conducted at the OMEGA-EP laser facility at the Laboratory for Laser Energetics [35]. A 51  $\mu$ m thick polycrystalline silicon sample was shock-compressed to  $\sim 100\,\mathrm{GPa}$  using a single drive laser beam delivering  $\sim 440\,\mathrm{J}$  over 10 ns with a  $\sim 1.1\,\mathrm{mm}$  diameter distributed phase plate. The drive laser is incident on a 11  $\mu$ m polystyrene (C<sub>8</sub>H<sub>8</sub>) ablator at a 19.3° angle with respect to the target normal. The ablator was fixed to the front of the silicon sample using a thin layer of glue ( $< 1\,\mu$ m). Three additional beams were tightly focused on a 12.5  $\mu$ m thick copper backlighter with an areal size of 4 mm<sup>2</sup>, generating a 1 ns pulse of Cu He-alpha X-rays centered at  $E\sim 8.4\,\mathrm{keV}$  [36]. The X-ray source was placed  $\sim 17\,\mathrm{mm}$  away from the silicon sample.

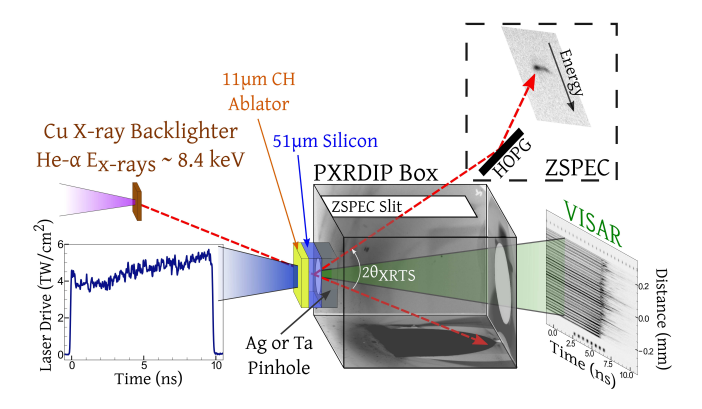


FIG. 1. Experimental setup at the OMEGA-EP laser facility. The silicon target is mounted on the front of the PXRDIP box [38] with a 100  $\mu \rm m$  thick, 0.5 mm diameter Ag or Ta pinhole. A single beam drives the CH-Si target with a tailored pulse as shown in the inset figure. The remaining three lasers generate Cu He- $\alpha$  X-rays. The red dashed lines represent the scattered X-ray paths that are collected by the XRTS and XRD IPs. The raw data shown were collected from s30967. NB: Not drawn to scale.

The experimental configuration devised to probe the structure of WDM silicon at OMEGA-EP is shown in Figure 1. It employed a variation of the powder X-ray diffraction image plate (PXRDIP) setup [25], which uses Fujifilm BAS-MS image plates (IP's) [37]. Due to spatial constraints the X-ray diffraction only accessed momentum transfers up to  $k \sim 4 \text{ Å}^{-1}$  at 8.4 keV. To extend the capabilities of the PXRDIP diagnostic, OMEGA's Bragg crystal spectrometer (ZSPEC) was added to measure scattering at high momentum transfer, and is capable of resolving the electronic structure of sufficiently ionized systems. The ZSPEC consists of a  $25 \,\mathrm{mm} \times 50 \,\mathrm{mm}$ highly-oriented pyrolitic graphite (HOPG) crystal with a radius of curvature of 27 mm, and placed 12.8 cm after the sample. As shown in the top inset in Figure 1, the ZSPEC was fielded out of perfect von-Hamos focusing meaning the X-rays were spectrally dispersed on a curve. The spectral analysis procedure can be found in the Supplementary Material. The silicon sample was fitted to the front of the PXRDIP enclosure on top of a 0.5 mm diameter silver or tantalum collimating aperture pinhole, which restricts the diagnostics' line-of-sight to the central planar shock region. These materials were chosen to ensure no fluorescence within the ZSPEC energy range, and to reduce interference between the pinhole and silicon Bragg peaks on the PXRDIP.

To measure the shock-breakout (SBO) time we fielded line-imaging VISAR which monitored the silicon sample's free surface [39]. The streaked image inset in Figure 1 shows the SBO as a rapid disappearance of the fringes around  $\sim 5\,\mathrm{ns}$ . As silicon is opaque to the VISAR wavelength (532 nm) at the investigated conditions, direct measurements of shock and particle velocity are only

achievable by employing witnesses and pressure windows. However, introducing these materials is unsuitable for scattering measurements due to the significant resultant contamination, making it difficult to isolate the scattering signal from the liquid silicon. Instead, utilizing the bilinear relationship in Ref. [27], which for small velocities is calculated from previous high explosive measurements [40], the silicon shock velocity is determined as  $9.5 \pm 0.2 \, \mathrm{km/s}$ . Combining this with the Rankine-Hugoniot relations, we measured the achieved pressuredensity state to be  $101 \pm 6 \, \mathrm{GPa}$  and  $4.43 \pm 0.08 \, \mathrm{g/cm^3}$ .

At these conditions silicon is expected to be in the fluid state, which occurs when dynamically compressed above 30 GPa [14, 41]. Whilst liquid silicon scattering, up to 30 GPa, has been previously observed at XFELs [14], extracting the contribution from low-Z liquids at high-power laser facilities is experimentally challenging due to limited X-ray source brightness, the presence of fluorescence, spurious scattering from the pinhole, and X-ray emission in the drive ablation plasma. To achieve this we quantified the contribution from the pinhole, ablation plasma and ambient sample. The procedure is described in detail in the Supplementary Material.

As shown in Figure 2(a), a broad scattering feature, attributed to liquid silicon, is observed around  $2\theta \sim 45^{\circ}$ . Due to the PXRDIP's geometry and the broad band X-ray emission from the laser generated plasma plume, shadows from the box appear on the IP's, preventing a complete azimuthal integration in  $\phi$ -space. Instead, a partial integration is performed by selecting regions with reduced contamination from the aforementioned sources. The resultant signal for a reference shot (s30970), which contained only the pinhole and ablator, and a driven silicon sample (s30967) are shown in Figure 2(b) in green and blue, respectively. The final liquid silicon scattering signal,  $I_{liq}(k)$ , shown in Figure 3(a) is obtained by subtracting the reference shot from the driven sample, and excluding the  $2\theta$  regions around the pinhole Bragg peaks. Further details can be found in the Supplementary Material. A  $2\theta$  error of  $\sim 0.5^{\circ}$  is taken to be the average deviation of the observed pinhole Bragg peaks from their expected values.

Additionally, the fraction of shocked (fluid) material within the probe volume was inferred using the ZSPEC diagnostic by comparing data obtained with varying time delays between the drive laser and X-ray probe. As the volume of liquid silicon increases, the elastic scattering signal recorded on the XRTS, fielded in-between Bragg peaks, becomes more intense. From the elastic signal measured on s30967, the volume fraction was found to be  $\sim 0.6$  (see Supplementary Material). Due to the low ionization of the liquid silicon, an inelastic scattering feature was not resolved above the ZSPEC instrumental noise.

At high momentum transfers the liquid scattering signal is the result of coherent,  $I_{\text{coh}}(k)$ , incoherent,  $I_{\text{incoh}}(k)$ , and multiple,  $I_{\text{m}}(k)$ , scattering. As the silicon thickness

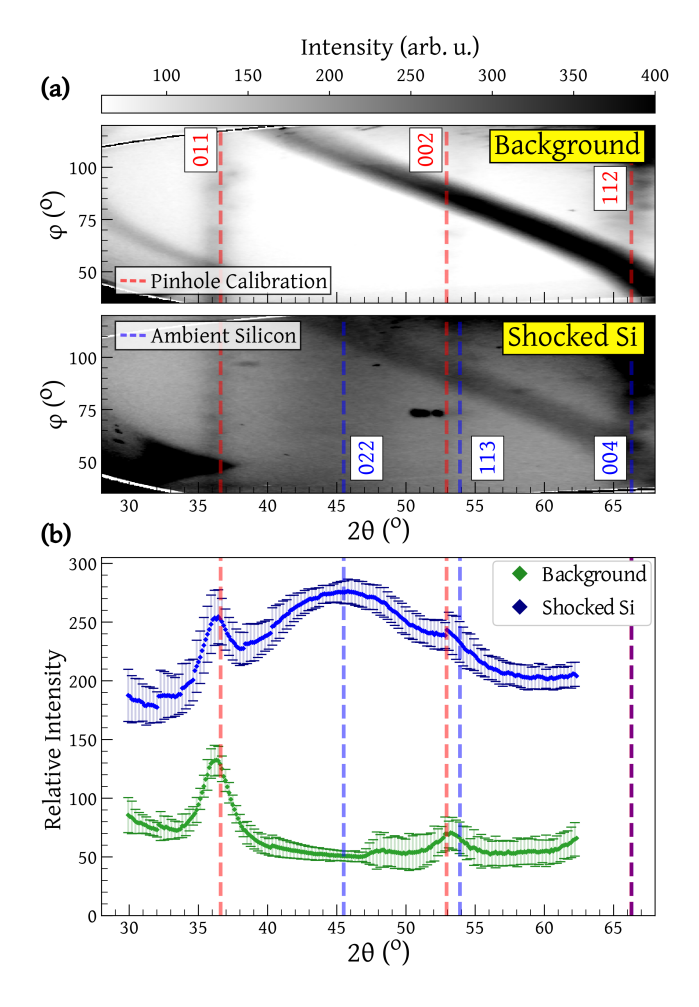


FIG. 2. (a) X-ray diffraction data, projected into  $2\theta$ - $\phi$  space (see Supplementary Material) [38], from background shot s30970, where no Si was placed in the target holder, and the liquid Si diffraction from s30967. The superimposed red and blue dashed vertical lines are the expected  $2\theta$  Bragg diffraction peaks of the Ta pinhole and ambient silicon, respectively. (b) Relative intensities of the partial- $\phi$  integrated scattering shown for the background (in green) and shock-compressed silicon (in blue) shots.

is small relative to its attenuation length,  $I_{\rm m}(k)$  is assumed to be negligible. The experimentally measured  $I_{\rm liq}(k)$  is related to the normalized ion-ion structure factor,  $S_{\rm ii}(k)$ , via [42, 43],

$$\frac{I_{\rm liq}(k)}{\gamma} \equiv I_{\rm scal}(k) = I_{\rm coh}(k) \left[ S_{\rm ii}(k) - 1 \right] + \left[ I_{\rm coh}(k) + I_{\rm incoh}(k) \right], \quad (1)$$

where  $I_{\rm coh}(k) = |f(k) + q(k)|^2$ , with f(k) the form factor of the tightly bound electrons and q(k) that of the free electrons that follow the ion motion [44]. The factor  $\gamma$  is a scaling constant defined such that  $I_{\rm scal}(k \to \infty) = I_{\rm coh}(k) + I_{\rm incoh}(k)$ . To be experimentally obtained, momentum transfers in excess of  $10\,\text{Å}^{-1}$  are required, a regime not currently accessible at high-power laser fa-

cilities. Here,  $I_{\rm incoh}(k)$  is obtained using the tabulated values from Ref. [45] and  $I_{\rm coh}(k)$  is simulated using the multi-component scattering spectra (MCSS) code [46]. As detailed further in the Supplementary Material,  $\gamma$  is left proportional to a free random Gaussian scalar with a standard deviation equal to the noise of the raw data.

The large parameter space,  $\Psi(\rho,T,Z)$ , is explored using a Markov-Chain Monte Carlo (MCMC) procedure [47, 48]. This uses Bayesian inference to determine the likelihood of a set of parameters producing the experimental spectrum based on an acceptance percentage

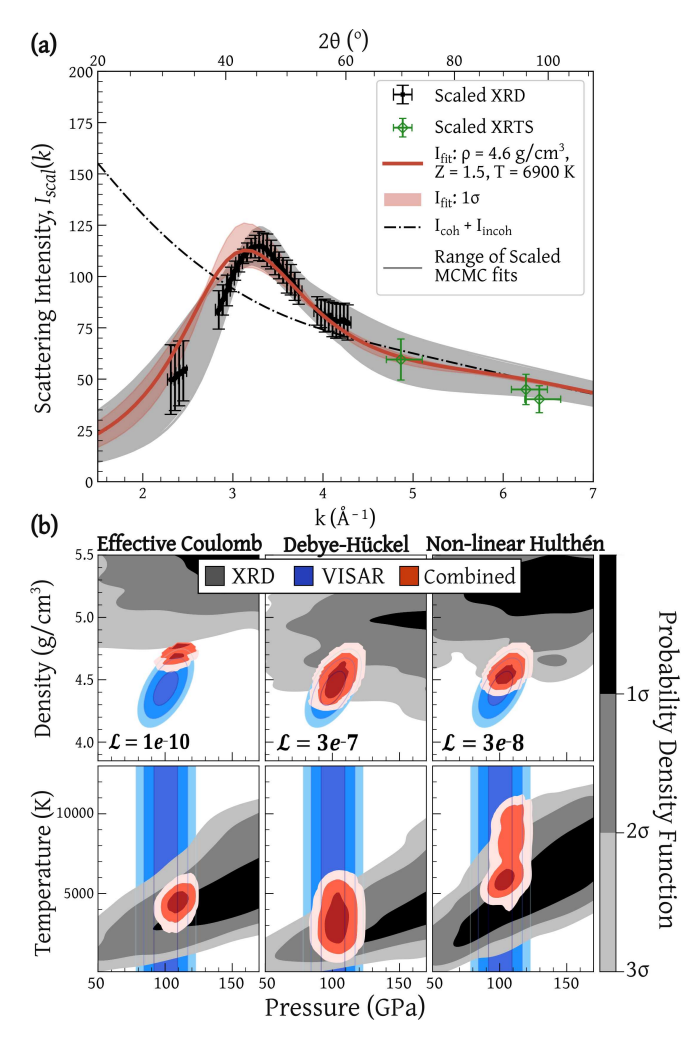


FIG. 3. (a) Liquid Si diffraction signal,  $I_{\rm scal}(k)$ , (in blue) is shown scaled to the theoretical signal,  $I_{\rm fit}(k)$ , (thick red line) produced by the combined VISAR and converged MCMC conditions using the non-linear Hulthén model. The  $1\sigma$  error of  $I_{\rm fit}(k)$  is shaded in red. The dash-dotted black line shows  $I_{\rm coh}+I_{\rm incoh}$  for these values. The broad range of accepted MCMC fits (in gray) are scaled to the mean fit. (b) Probability density functions in the P- $\rho$  and P-T phase for VISAR (blue heat maps) and X-ray scattering (gray heat maps) analysis using each  $V_{ii}$ . The corresponding joint distributions are superimposed as red heat maps. In the upper grid the likelihood, as defined in equation 3, of each  $V_{ii}$  is shown.

 $P[I_{\text{scal}}(k)|\Psi] = e^{-\beta_{\text{cost}}}$  with

$$\beta_{\text{cost}} = \max \left[ \frac{I_{\text{fit}}(k) - I_{\text{scal}}(k)}{\sqrt{2}\sigma\Sigma} \right]^2,$$
(2)

where  $\Sigma$  is the error on  $I_{\rm scal}$ , and  $\sigma=0.5$  is a scalar chosen to allow acceptance freedom within data uncertainty. The investigated parameter space assumed a uniform distribution with linear sampling for the density,  $2.33 \leq \rho \, ({\rm g/cm^3}) \leq 6$ , ionization,  $0 \leq Z \leq 14$ , and temperature,  $10^3 \leq T_e = T_i \, ({\rm K}) \leq 1.1 \times 10^4$ .

Simulating  $S_{ii}(k)$ , however, is subject to model biases and requires appropriate selection of electron and ion interactions. Measurement of the liquid structure factor opens the opportunity for direct model compar-

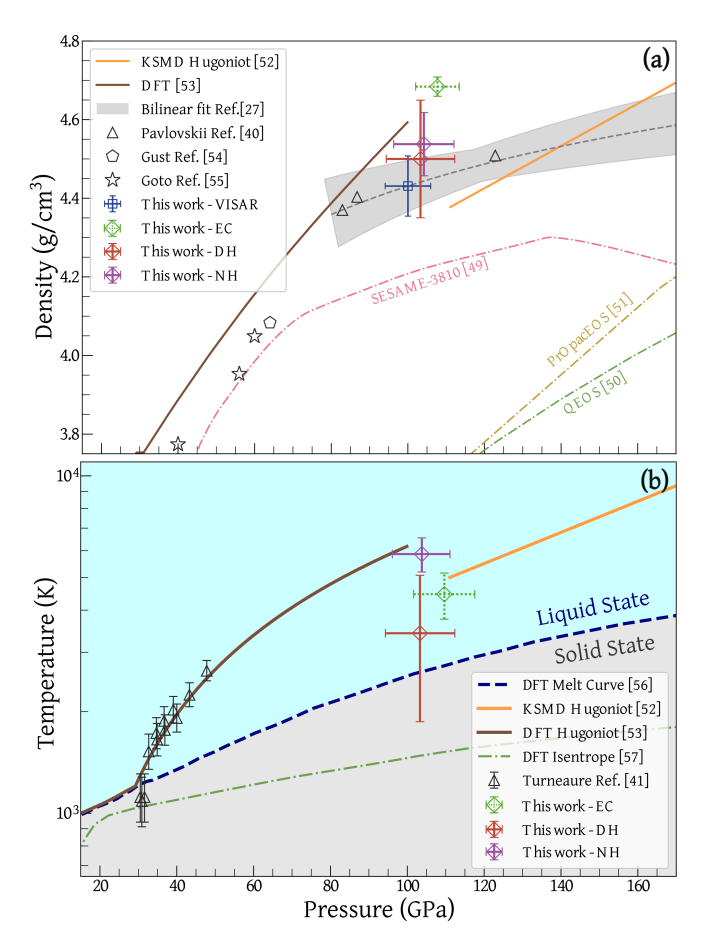


FIG. 4. (a) The principal silicon Hugoniot where this work is compared to SESAME-3810, [49], quotidian equation-of-state (QEOS) [50], PrOpacEOS [51], ab initio Kohn-Sham DFT molecular-dynamics (KSMD) [52], principle Hugoniot from DFT [53], and previous experimental work collected via conservation methods [40, 54, 55]. The bilinear fit [27] used to infer particle velocity is shown as a filled gray bar. (b) The silicon pressure-temperature phase diagram comparing the combined  $1\sigma$  error for each  $V_{ii}$  to the measured and predicted melt curve [56], the DFT isentrope [57] and previous shocked silicon experiments [41] where the temperature was inferred using molecular dynamics [58].

ison. In the partially ionized, low density state, the ion-ion interaction potential,  $V_{ii}(k)$  is commonly modeled using Debye-Hückel (DH) [59]. This work compares the DH model with the bare (unscreened) effective Coulomb (EC) interaction and a model non-linear Hulthén (NH) interaction [60]; the latter approximately describes screening beyond the DH approach. For the screening cloud, q(k), large momentum transfers in high-density matter have shown deviation from the simple DH model as a result of finite-wavelength screening (FWS) [61]. As detailed in the Supplementary Material, the simulated liquid scattering is comparatively insensitive to each q(k) model and FWS was chosen for the MCMC analysis.

In Figure 3(a) the range of accepted fits after MCMC convergence using the NH model are shown in gray. The signal from the XRTS recorded on shots that were probed after shock breakout (where the liquid volume fraction > 0.9) are compared in green against the angularly resolved scattering in Figure 3(a), extending the effective k range. While these points were not included in the MCMC fitting process due to the lack of an absolute signal intensity calibration between XRD and XRTS, they nonetheless exhibit good agreement with the results.

Using a suitable theoretical description, the plasma pressure can be determined from the range of accepted fits. Under conditions of strongly coupled ions and degenerate electrons, where screening is expected to be significant, a reasonable framework is the 'two-fluid' model discussed by Vorberger et al. [62, 63] (see Supplementary Material). The converged probability density functions  $Pr(P, \rho)$  and Pr(P, T), for each  $V_{ii}$ , are shown in gray in Figure 3(b) and compared, in blue, to the  $P-\rho$  state inferred using VISAR. Combining these concurrent diagnostics we find the joint  $P-\rho$  probability density functions, superimposed in Figure 3(b) as red heat maps. The relatively small overlap between the VISAR and XRD PDFs highlights the distinct information each diagnostic is sensitive to. By combining their PDFs therefore, we gain a more comprehensive understanding of the shockcompressed conditions by constraining the XRD parameter search to those consistent with the pressure-density Hugoniot relation established by the VISAR measurement.

The likelihood of each  $V_{ii}$  model given the VISAR information is defined as the sum of its joint probability distribution,

$$\mathcal{L}(V_{ii}|\text{VISAR}) = \sum_{\rho,P} \Pr_m(P,\rho) \times \Pr_v(P,\rho), \quad (3)$$

where m and v denote the MCMC and VISAR probability density functions, respectively. These likelihoods are indicated in the upper grid of Figure 3(b). They show that comparatively, the effective-Coulomb model is a poor representation of the liquid silicon state. This is expected as it does not account for screening effects.

Unlike the VISAR diagnostic, the MCMC convergence of the X-ray scattering analysis is dependent not only on pressure and density, but also on temperature. Propagating the combined  $\Pr(P,\rho)$  into temperature space re-distributes the X-ray scattering  $\Pr(P,\rho,T)$  to penalize where the density and pressure disagree with VISAR. The resultant  $\Pr(P,\rho,T)$  are used to find the combined  $1\sigma$  errors in the pressure-temperature phase, shown in red in the lower grid of Figure 3(b). The simulated X-ray diffraction fits,  $I_{\rm fit}$ , produced by the conditions inferred when combining VISAR and the NH MCMC convergence are shown in red in Figure 3(a).

In Figure 4 the VISAR and MCMC combined  $1\sigma$  P- $\rho$  and P-T for each  $V_{ii}$  model are plotted on the principal Hugoniot. Despite having the closest agreement with VISAR in P- $\rho$ , the temperature predicted by the Debye-Hückel model falls below the Hugoniot state. Instead we find the implementation of a Hulthén potential [60], which estimates non-linear screening regimes beyond DH, better describes the thermodynamic conditions. This platform therefore demonstrates the capability to effectively distinguish between screening models which is essential for accurately predicting material behavior under extreme conditions.

This report presents detailed insights into the extreme states of matter generated at high-power laser facilities. While previous studies on liquid silicon have been confined to pressures around  $\sim 50 \,\mathrm{GPa}$  [14, 41], the combination of multiple in situ diagnostics, along with MCMC analysis, effectively reduces diagnostic biases and yielded uncertainties on the shock-compressed state that are comparable to previous experimental work, without relying on EOS models. Furthermore, the synergistic combination of diagnostics facilitated the differentiation of distinct static screening models. The results revealed the necessity of incorporating screening beyond the linear Debye-H"uckel approach, employing a Hulth'en potential, to achieve agreement between the measured liquid silicon state and Hugoniot predictions. Therefore, this platform paves the way for exploring the structure of HED matter at high-power laser facilities.

This material is based upon work supported by the Department of Energy National Nuclear Security Administration under Award Number DE-NA0003856, the University of Rochester, and the New York State Energy Research and Development Authority and the National Science Foundation under Grant No. PHY-2045718. Part of this work was prepared by LLNL under Contract No. DE-AC52-07NA27344. The PXRDIP data was analyzed with LLNL AnalyzePXRDIP package.

This report was prepared as an account of work sponsored by an agency of the U.S. Government. Neither the U.S. Government nor any agency thereof, nor any of their employees, makes any warranty, express or implied, or assumes any legal liability or responsibility for the accuracy, completeness, or usefulness of any information,

apparatus, product, or process disclosed, or represents that its use would not infringe privately owned rights. Reference herein to any specific commercial product, process, or service by trade name, trademark, manufacturer, or otherwise does not necessarily constitute or imply its endorsement, recommendation, or favoring by the U.S. Government or any agency thereof. The views and opinions of authors expressed herein do not necessarily state or reflect those of the U.S. Government or any agency thereof.

- $^*$  hannah.poole@physics.ox.ac.uk
- A. Benuzzi-Mounaix, S. Mazevet, A. Ravasio, T. Vinci,
   A. Denoeud, M. Koenig, N. Amadou, E. Brambrink,
   F. Festa, A. Levy, et al., Physica Scripta 2014, 014060 (2014).
- [2] T. G. Sharp and P. S. DeCarli, Meteorites and the early solar system II **943**, 653 (2006).
- [3] F. Graziani, M. P. Desjarlais, R. Redmer, and S. B. Trickey, Frontiers and challenges in warm dense matter, vol. 96 (Springer Science & Business, 2014).
- [4] R. S. Craxton, K. S. Anderson, T. R. Boehly, V. N. Goncharov, D. R. Harding, J. P. Knauer, R. L. McCrory, P. W. McKenty, D. D. Meyerhofer, J. F. Myatt, et al., Physics of Plasmas 22, 110501 (2015).
- [5] S. X. Hu, L. A. Collins, T. R. Boehly, Y. H. Ding, P. B. Radha, V. N. Goncharov, V. V. Karasiev, G. W. Collins, S. P. Regan, and E. M. Campbell, Physics of Plasmas 25, 056306 (2018).
- [6] M. Landeau, A. Fournier, H.-C. Nataf, D. Cébron, and N. Schaeffer, Nature Reviews Earth & Environment 3, 255 (2022).
- [7] J. Badro, A. S. Côté, and J. P. Brodholt, Proceedings of the National Academy of Sciences 111, 7542 (2014).
- [8] F. Soubiran, B. Militzer, K. P. Driver, and S. Zhang, Physics of Plasmas 24, 041401 (2017).
- [9] G. A. de Wijs, G. Kresse, L. Vočadlo, D. Dobson, D. Alfe,M. J. Gillan, and G. D. Price, Nature 392, 805 (1998).
- [10] S. H. Glenzer, L. B. Fletcher, E. Galtier, B. Nagler, R. Alonso-Mori, B. Barbrel, S. B. Brown, D. A. Chapman, Z. Chen, C. B. Curry, et al., Journal of Physics B: Atomic, Molecular and Optical Physics 49, 092001 (2016)
- [11] M. Koenig, A. Benuzzi-Mounaix, A. Ravasio, T. Vinci, N. Ozaki, S. Pape, D. Batani, G. Huser, T. Hall, D. Hicks, et al., Plasma Physics and Controlled Fusion 47, B441 (2005).
- [12] K. Wünsch, J. Vorberger, G. Gregori, and D. O. Gericke, Europhysics Letters 94, 25001 (2011).
- [13] L. B. Fletcher, H. J. Lee, T. Döppner, E. Galtier, B. Nagler, P. Heimann, C. Fortmann, S. L. Pape, T. Ma, M. Millot, et al., Nature photonics 9, 274 (2015).
- [14] E. E. McBride, A. Krygier, A. Ehnes, E. Galtier, M. Harmand, Z. Konôpková, H. J. Lee, H.-P. Liermann, B. Nagler, A. Pelka, et al., Nature Physics 15, 89 (2019).
- [15] S. Brygoo, P. Loubeyre, M. Millot, J. Rygg, P. Celliers, J. Eggert, R. Jeanloz, and G. Collins, Nature 593, 517 (2021).
- [16] H. Abu-Shawareb, R. Acree, P. Adams, J. Adams, B. Ad-

- dis, R. Aden, P. Adrian, B. Afeyan, M. Aggleton, L. Aghaian, et al., Physical Review Letters **129**, 075001 (2022).
- [17] M. Bonitz, T. Dornheim, Z. A. Moldabekov, S. Zhang, P. Hamann, H. Kählert, A. Filinov, K. Ramakrishna, and J. Vorberger, Physics of Plasmas 27, 042710 (2020).
- [18] S. X. Hu, W. Theobald, P. B. Radha, J. L. Peebles, S. P. Regan, A. Nikroo, M. J. Bonino, D. R. Harding, V. N. Goncharov, N. Petta, et al., Physics of Plasmas 25, 082710 (2018).
- [19] D. Kraus, D. A. Chapman, A. L. Kritcher, R. A. Baggott, B. Bachmann, G. W. Collins, S. H. Glenzer, J. A. Hawreliak, D. H. Kalantar, O. L. Landen, et al., Physical Review E 94, 011202(R) (2016).
- [20] P. Davis, T. Döppner, J. R. Rygg, C. Fortmann, L. Divol, A. Pak, L. Fletcher, A. Becker, B. Holst, P. Sperling, et al., Nature communications 7, 11189 (2016).
- [21] S. P. Regan, K. Falk, G. Gregori, P. B. Radha, S. X. Hu, T. R. Boehly, B. J. B. Crowley, S. H. Glenzer, O. L. Landen, D. O. Gericke, et al., Physical review letters 109, 265003 (2012).
- [22] H. J. Lee, P. Neumayer, J. Castor, T. Döppner, R. W. Falcone, C. Fortmann, B. A. Hammel, A. L. Kritcher, O. L. Landen, R. W. Lee, et al., Physical review letters 102, 115001 (2009).
- [23] A. Lazicki, J. R. Rygg, F. Coppari, R. Smith, D. Fratanduono, R. G. Kraus, G. W. Collins, R. Briggs, D. G. Braun, D. C. Swift, et al., Physical review letters 115, 075502 (2015).
- [24] F. Coppari, D. E. Fratanduono, M. Millot, R. G. Kraus, A. Lazicki, J. R. Rygg, R. F. Smith, and J. H. Eggert, Physical Review B 106, 134105 (2022).
- [25] J. R. Rygg, J. H. Eggert, A. E. Lazicki, F. Coppari, J. A. Hawreliak, D. G. Hicks, R. F. Smith, C. M. Sorce, T. M. Uphaus, B. Yaakobi, et al., Review of Scientific Instruments 83, 113904 (2012).
- [26] X. Gong, D. N. Polsin, R. Paul, B. J. Henderson, J. H. Eggert, F. Coppari, R. F. Smith, J. R. Rygg, and G. W. Collins, Physical Review Letters 130, 076101 (2023).
- [27] B. J. Henderson, M. C. Marshall, T. R. Boehly, R. Paul, C. A. McCoy, S. X. Hu, D. N. Polsin, L. E. Crandall, M. F. Huff, D. A. Chin, et al., Physical Review B 103, 094115 (2021).
- [28] K. Falk, S. P. Regan, J. Vorberger, B. J. B. Crowley, S. H. Glenzer, S. X. Hu, C. D. Murphy, P. B. Radha, A. P. Jephcoat, J. S. Wark, et al., Physical Review E 87, 043112 (2013).
- [29] E. J. Davies, P. J. Carter, S. Root, R. G. Kraus, D. K. Spaulding, S. T. Stewart, and S. B. Jacobsen, Journal of Geophysical Research: Planets 125, e2019JE006227 (2020).
- [30] K. Hirose, G. Morard, R. Sinmyo, K. Umemoto, J. Hernlund, G. Helffrich, and S. Labrosse, Nature 543, 99 (2017).
- [31] G. Huser, N. Ozaki, P. Colin-Lalu, V. Recoules, T. Sano, Y. Sakawa, K. Miyanishi, and R. Kodama, Physics of Plasmas 25, 052706 (2018).
- [32] M. J. Edwards, J. D. Lindl, B. K. Spears, S. V. Weber, L. J. Atherton, D. L. Bleuel, D. K. Bradley, D. A. Callahan, C. J. Cerjan, D. Clark, et al., Physics of Plasmas 18, 051003 (2011).
- [33] S. X. Hu, G. Fiksel, V. N. Goncharov, S. Skupsky, D. D. Meyerhofer, and V. A. Smalyuk, Physical Review Letters 108, 195003 (2012).

- [34] G. Fiksel, S. X. Hu, V. A. Goncharov, D. D. Meyerhofer, T. C. Sangster, V. A. Smalyuk, B. Yaakobi, M. J. Bonino, and R. Jungquist, Physics of Plasmas 19, 062704 (2012).
- [35] D. D. Meyerhofer, J. Bromage, C. Dorrer, J. H. Kelly, B. E. Kruschwitz, S. J. Loucks, R. L. McCrory, S. F. B. Morse, J. F. Myatt, P. M. Nilson, et al., Journal of Physics: Conference Series 244, 032010 (2010).
- [36] F. Coppari, R. F. Smith, D. B. Thorn, J. R. Rygg, D. A. Liedahl, R. G. Kraus, A. Lazicki, M. Millot, and J. H. Eggert, Review of Scientific Instruments 90, 125113 (2019).
- [37] A. L. Meadowcroft, C. D. Bentley, and E. N. Stott, Review of scientific instruments 79, 113102 (2008).
- [38] J. R. Rygg, R. F. Smith, A. E. Lazicki, D. G. Braun, D. E. Fratanduono, R. G. Kraus, J. M. McNaney, D. C. Swift, C. E. Wehrenberg, F. Coppari, et al., Review of Scientific Instruments 91, 043902 (2020).
- [39] P. M. Celliers and M. Millot, Review of Scientific Instruments 94, 011101 (2023).
- [40] M. N. Pavlovskii, Soviet Physics Solid State 9, 2514 (1968).
- [41] S. J. Turneaure, S. M. Sharma, and Y. M. Gupta, Physical review letters 121, 135701 (2018).
- [42] J. W. E. Drewitt, Journal of Physics: Condensed Matter 33, 503004 (2021).
- [43] S. Singh, A. L. Coleman, S. Zhang, F. Coppari, M. G. Gorman, R. F. Smith, J. H. Eggert, R. Briggs, and D. E. Fratanduono, Journal of Synchrotron Radiation 29, 1033 (2022).
- [44] J. Chihara, Journal of Physics: Condensed Matter 12, 231 (2000).
- [45] J. H. Hubbell, W. J. Veigele, E. A. Briggs, R. T. Brown, D. T. Cromer, and R. J. Howerton, Journal of physical and chemical reference data 4, 471 (1975).
- [46] D. A. Chapman, User Guide and Theoretical Basis for the Multi-Component Scattering Spectra (MCSS) Thomson Scattering Analysis Code (AWE, 2017).
- [47] M. Kasim, T. P. Galligan, J. Topp-Mugglestone, G. Gregori, and S. M. Vinko, Physics of Plasmas 26, 112706 (2019).
- [48] H. Poole, R. E. D. Cao, I. Golovkin, T. Walton, S. X. Hu, M. Kasim, S. M. Vinko, J. R. Rygg, V. N. Goncharov, G. Gregori, et al., Physics of Plasmas 29, 072703 (2022).
- [49] B. I. Bennett, J. D. Johnson, G. I. Kerley, and G. T. Rood, Los Alamos National Laboratory, Los Alamos, NM pp. LA-7130 (1978).
- [50] R. M. More, K. H. Warren, D. A. Young, and G. B. Zimmerman, The Physics of fluids 31, 3059– (1988).
- [51] J. J. MacFarlane, I. E. Golovkin, and P. R. Woodruff, Journal of Quantitative Spectroscopy and Radiative Transfer 99, 381 (2006).
- [52] S. X. Hu, B. Militzer, L. A. Collins, K. P. Driver, and J. D. Kress, Physical Review B 94, 094109 (2016).
- [53] R. Paul, S. X. Hu, and V. V. Karasiev, Physical Review B 100, 144101 (2019).
- [54] W. H. Gust and E. B. Royce, Journal of Applied Physics 42, 1897 (1971).
- [55] T. Goto, T. Sato, and Y. Syono, Japanese Journal of Applied Physics 21, L369 (1982).
- [56] R. Paul, S. X. Hu, and V. V. Karasiev, Physical Review Letters 122, 125701 (2019).
- [57] R. Paul, Private Communication (2022).
- [58] O. Strickson and E. Artacho, Physical Review B 93, 094107 (2016).
- [59] P. Debye and E. Hückel, Physikalische Zeitschrift 24, 185

- (1923).
- [60] Y. P. Varshni, Physical Review A 41, 4682 (1990).
- [61] D. A. Chapman, J. Vorberger, L. B. Fletcher, R. A. Baggott, L. Divol, T. Döppner, R. W. Falcone, S. H. Glenzer, G. Gregori, T. M. Guymer, et al., Nature communications 6, 6839 (2015).
- [62] J. Vorberger, D. O. Gericke, and W.-D. Kraeft, High Energy Density Physics 9, 448 (2013).
- [63] W. Ebeling, H. Reinholz, and G. Röpke, The European Physical Journal Special Topics **229**, 3403 (2020).
- [64] See Supplementary Material, [URL], which includes Refs. [65–71] therein.
- [65] A. Pak, G. Gregori, J. Knight, K. Campbell, D. Price, B. Hammel, O. L. Landen, and S. H. Glenzer, Review of Scientific Instruments 75, 3747 (2004).
- [66] A. Pelka, G. Gregori, D. O. Gericke, J. Vorberger, S. H. Glenzer, M. M. Gunther, K. Harres, R. Heathcote, A. L.

- Kritcher, N. L. Kugland, et al., Physical review letters **105**, 265701 (2010).
- [67] M. A. Barrios, D. G. Hicks, T. R. Boehly, D. E. Fratanduono, J. H. Eggert, P. M. Celliers, G. W. Collins, and D. D. Meyerhofer, Physics of Plasmas 17, 056307 (2010).
- [68] D. A. Chapman, D. Kraus, A. L. Kritcher, B. Bachmann, G. W. Collins, R. W. Falcone, J. A. Gaffney, D. O. Gericke, S. H. Glenzer, T. M. Guymer, et al., Physics of Plasmas 21, 082709 (2014).
- [69] S. Groth, T. Dornheim, T. Sjostrom, F. D. Malone, W. M. C. Foulkes, and M. Bonitz, Physical review letters 119, 135001 (2017).
- [70] T. Dornheim, Z. A. Moldabekov, and P. Tolias, Physical Review B 103, 165102 (2021).
- [71] J.-P. Hansen and I. R. McDonald, Theory of simple liquids: with applications to soft matter (Academic press, 2013).